AMERICAN
METEOROLOGICAL
SOCIETY

Journal of Physical Oceanography

The DOI for this manuscript is doi: 10.1175/JPO-D-14-0257.1

The final published version of this manuscript will replace the preliminary version at the above DOI once it is available.

If you would like to cite this EOR in a separate work, please use the following full citation:

Wahlin, A., O. Kalén, K. Assmann, E. Darelius, H. Ha, T. Kim, and S. Lee, 2015: Sub-inertial oscillations on the Amundsen Sea shelf, Antarctica. J. Phys. Oceanogr. doi:10.1175/JPO-D-14-0257.1, in press.

Sub-inertial oscillations on the Amundsen Sea shelf, Antarctica

A. K. Wåhlin*, O. Kalén, K. M. Assmann, E. Darelius, H. K. Ha, T. W. Kim, S. H. Lee

Abstract

Mooring data from the western flank of Dotson Trough, Amundsen Sea shelf region, show the presence of barotropic oscillations with a period of 40-80 hours. The oscillations are visible in velocity, temperature, salinity and pressure, and are comparable to tides in magnitude. The period of the oscillations corresponds to topographic Rossby waves of low group velocity and wavelength about 40 km, i.e. the half-width of the channel. It is suggested that these resonant topographic Rossby waves cause the observed peak in the wave spectra. The observations show that sparse CTD data from this region should be treated with caution and need to be complemented with moorings or yo-yo stations in order to give a representative picture for the hydrography.

* Corresponding author

Dr. A. K. Wåhlin
Department of Earth Sciences
University of Gothenburg
PB 460
405 30 Göteborg
Sweden

Phone: +46 31 786 2866
Email: awahlin@gu.se

1. Introduction.

Rapidly melting ice shelves and inflow of warm water on the continental shelf sea in the Amundsen Sea have brought attention and increased research activity to the region, and the knowledge about the circulation in the area has increased substantially over the last decade. Figure 1 shows a partial map of the Amundsen shelf area. It is cross-cut by three deep troughs; the Pine Island trough which branches out in two distinct exits and the Dotson trough with one main exit on the shelf break. These troughs channel relatively warm and salty water southward (Wåhlin et al, 2010; Walker et al, 2007) from the deep ocean towards the floating glaciers at the coast where it induces basal melt (e.g. Jenkins et al, 2010; Jacobs et al, 2011). The focus of this paper is the Dotson trough, where records from two current meter moorings (Fig 1. and Table 1) deployed on the flanks of the trough reveal a persistent inflow of warm and salty deep water (Wåhlin et al, 2010; Arneborg et al, 2012; Wåhlin et al, 2013; Ha et al, 2014) on the eastern flank, and an outflow of colder and fresher product waters on the western flank (Ha et al, 2014). The circulation pathway of the deep water (thick lines with arrows in Figure 1) was investigated by Ha et al (2014) and it was shown that the inflow has velocity-weighted average temperature of about 0.75 ^{o}C and salinity 34.6 psu. From budget calculations based on the mooring data it was found that the outflow current was 1.25°C colder and 0.3 psu fresher than the inflow due to mixing with glacial melt water,which corresponds to melting about 80 - 240 km^3 glacial ice per year. The overturning time was estimated to 4 months. In both moorings, a strong short-term variability dominates the time dependence in velocity, temperature and salinity. On the eastern flank the velocity varied on time scales from sub tidal up to monthly, was correlated with eastward wind at the shelf break (Wåhlin et al, 2013), and had no pronounced seasonality. A weak wintertime maximum in the bottom temperature and CDW layer thickness was however observed which was not related to the velocity (Wåhlin et al, 2013; Ha et al, 2014).

The focus of this work will be the quasi-regular oscillations with a period of about 2.5 days that are found at the site of a mooring located on the western flank of the trough, i.e. the outflow side. The instantaneous velocity and hydrography is dominated by these oscillations. It is suggested that the oscillations are due to resonant topographic Rossby waves, which have previously been observed e.g. on the Scottish continental shelf (Gordon and Huthnance, 1987) and on the southern slope of the Iceland-Faroe ridge (Miller, Lermusiaux, & Poulain, 1996).

Topographic Rossby waves are a manifestation of conservation of potential vorticity: A water column forced to move across isobaths acquires relative vorticity (rotation) as it is stretched or squeezed. In the southern hemisphere, the phase of topographic Rossby waves propagates with shallow water on the left, while the energy of the wave follows the group velocity, which may be directed either to the right or to the left depending on the wavelength (Gill, 1987; Rhines, P., 2014: forthcoming textbook: http://www.ocean.washington.edu/courses/oc512/rossby-waves-gfd109-lec5a-07.pdf). For lower modes of the wave the dispersion curve typically displays a local maximum, with the group velocity of short waves directed with shallow water on the right and the group velocity of longer waves with shallow water on the left. For some intermediate wave-length, the group velocity is zero or close to zero. The energy of the latter waves will hence remain in the forcing region. These zero-group-velocity waves are said to be resonant, and such waves have been observed to be generated e.g. by strong winds (Gordon & Huthnance, 1987) or by tides (Padman, Plueddemann, Muench, & Pinkel, 1992).

Rossby waves are not eddies, and they do not transport any fluid. The streamlines are per definition closed. Hence they are not expected to influence transport of quantities such as heat or salt across the topography. The exception is when the waves are broken e.g. by small-scale topography (e.g. StLaurent et al, 2013) in which case a net flow can occur. Eddies on the other hand can translate and move fluid parcels, and they are in some regions (e.g. the Antarctic fronts) the main mechanism that induces horizontal mixing and transport properties such as heat and salt laterally (e.g Thompson, 2008; Thompson et al, 2014). In similarity with Rossby waves, eddies can give an oscillating signal in hydrographic measurements. Since they are fundamentally different with regard to whether they induce net motion of the fluid or not, it is important to distinguish the two mechanisms. The present results indicate that topographic Rossby waves are very frequently, in fact almost constantly, present in the western part of the outer Amundsen shelf area. These waves will likely contaminate any measurements made in this area indicating that single CTD and LADCP measurements from this region are of limited value.

2. Data.

The data presented in this study were collected during two cruises with *IB Oden* during austral summer 2009/2010 and 2010/2011 and two cruises with *RV Araon* during 2011/2012 and 2013/2014. Three bottom-mounted sub-surface moorings were placed in the western trough (Dotson Trough) crossing the Amundsen Sea shelf. Figure 1 shows a map of the region, the location of the three moorings (for exact position and times in water, see Table 1) and the mooring set-up. The position of mooring S1 was in the center of the warm inflow while S2 and S3 were positioned in the outflow zone on the western flank. The mooring lines contained between 3 and 7 MicroCATs (Seabird, SBE-37SMP) that measured temperature (with an accuracy of 0.002 K), conductivity (with an accuracy of 0.0003 S m^{-1}) and pressure (with an accuracy of 0.1 dbar). Two of the moorings also included an upward-looking 150-kHz Acoustic Doppler Current Profiler (ADCP; RDI), deployed at the bottom to measure current velocity profiles. The observed velocity data were processed using the WinADCP® software, removing data with error velocity exceeding 1.5 cm/s and beam correlation below 100. Fourier spectra were calculated using hourly time series and 50% overlapping Hanning windows with a length of 1024 h. The wind data used was the 6 hour ERA interim reanalysis product (Dee et al, 2011), which according to Bracegirdle and Marshall (2012) is the most accurate of the six major meteorological reanalysis products covering the Amundsen Sea. Bracegirdle and Marshall (2012) found generally good agreement between the ERA interim and independent data in the Bellingshausen Sea, and in Wåhlin et al (2013) a good agreement was found between ERA interim and in situ data from Lindsey Island.

3. Observations

The primary focus here is mooring S2, deployed for one year and equipped with an ADCP and 5 MicroCATs. Figure 2 shows the S2 temperature, salinity and channel-rotated (i.e. with a rotation angle of 30^{o} counterclockwise) velocities. In similarity with S1 (Wåhlin et al, 2013) there is a pronounced short-term variability in all these quantities that dominate the instantaneous fields. The bottom temperature can vary by up to 1^{o}C over less than a day, and the velocity by 15 cm/s in that time span. The velocity fluctuations are nearly constant in the vertical, and there is a weak wintertime maximum in bottom temperature. The long time mean along-channel velocity at S2 is an outflow of 2.5 cm/s, while the cross-channel component is weaker with a mean south-westward flow of less than 1 cm/s (Ha et al, 2014).

Figure 3 shows the Fourier spectra and the rotary spectra for the velocity at 100 m above bottom at S2. The velocity spectrum has marked peaks at the tidal frequencies, at the inertial frequency and a broad peak centered around period 40 - 80 hours. The shape and relative magnitude of the borad peak is approximately equal for all measured parameters at S2 (velocity, temperature, salinity). The oscillation is more energetic in the across trough direction and mainly clockwise (Fig 3).

In order to illustrate the temporal variation of the spectrum, wavelet analysis (according to Torrence and Compo, 1997) was used. Figure 4 shows the wavelet power spectra of bottom temperature and the vertically averaged velocities at S2. The peak around 40-80 hours is present in the vertically averaged velocities (Fig. 4a and 4b) as well as bottom temperature (Fig. 4c). The energy peak is present during the whole measurement period, and a few shorter periods with elevated energy can also be detected. The characteristics of these periods are largely similar. Figure 5 shows an example, a detailed view of the velocity and temperature starting at May 6th, 2011 (arrow in Figure 4). The oscillations are present in the whole water column below 330 m. Temperature co-oscillates with velocity, with dropping temperatures associated with south-westward currents across the channel and rising temperatures associated with north-eastward velocities indicating that the warm water layer close to the bottom is being moved up and down the slope by strong velocity oscillations. The oscillations have similar magnitude in both spatial directions.

Figure 6 shows the temperature from the three MicroCATs at mooring S3. In similarity with the temperature at S2, there is strong sub-inertial variability that dominates any instantaneous temperature measurements. The lower panels of Fig. 6 show two examples of temperature oscillations, resembling the event in Fig. 5. The power spectrum from the three MicroCATs show a broad subinertial peak similar to the one in Fig. 3 but centered around somewhat longer periods, around 70 - 100 hours.

In order to examine the coherence between wind and the S2 mooring velocity the spectral coherence between the vertically averaged currents and the wind pseudostress was calculated using the multi taper method (Thomson, 1982). The pseudostress was rotated in order to identify the angle with largest coherence. The maximum coherence of 0.69 (with confidence level 0.43) was found for frequency 67 hours and wind angle close to the local cross-shelf direction.

4. Topographic Rossby waves

Figure 7a shows the topography of the western flank of the trough, as measured by the multibeam on IB Oden during a cruise to the region in 2010 (Arndt et al, 2013; http://www.ibcso.org/data.html), together with a simplified topography *h(y)* with a constant bottom slope α, i.e.

$$h(y) = H_0 - \alpha y\,, \qquad (1)$$

where *h(y)* is the bottom elevation as a function of across-slope distance *y*; $H_0 = -250\ m$ and $\alpha = 0.01$.

Free topographic Rossby waves can form and travel along sloping topography. The shape of the wave (the eigenfunction) depends on the shape of the topography and the lateral boundary conditions. For the simplified topography (1), plane waves on the form

$$\Psi = \Psi_0 \sin(kx + ly - \omega t)\,, \qquad (2)$$

where *(k, l)* are the wave numbers in the *(x, y)* directions and ω is the frequency, are solutions to the linear barotropic wave equation (Rhines, P., 2014: forthcoming textbook:

http://www.ocean.washington.edu/courses/oc512/rossby-waves-gfd109-lec5a-07.pdf). The dispersion relation is given by

$$\omega = -\frac{\beta k}{k^2 + l^2 + \frac{f^2}{gH}}, \tag{3}$$

where $\beta = \frac{f\alpha}{H}$, f is the Coriolis parameter, g is the gravity and $H = H_0 - \frac{\alpha L}{2}$ is the average depth of the slope stretch. For the one-dimensional topography (1) the boundary conditions restrict which wave numbers are possible in the *y*-direction (i.e. the eigenvalues). For the boundary conditions

$$\begin{aligned} v &= 0 \quad \text{at } y = 0 \\ \frac{\partial v}{\partial y} &= 0 \quad \text{at } y = L \end{aligned}, \tag{4}$$

the solution (2) is valid for

$$l_n = (n + \frac{1}{2})\frac{\pi}{L}, \tag{5}$$

where n signifies mode number starting at zero so that the first mode is given by $l_0 = \frac{1}{2}\frac{\pi}{L}$ and the second by $l_1 = \frac{3}{2}\frac{\pi}{L}$.

A code for determining the eigenfunctions and modal structures numerically for a real topography and stratification was presented in Brink (2006) (see also http://www.whoi.edu/page.do?pid=23361), assuming an inviscid sea and a linear wave equation. Figure 7b shows the surface signature of the first and second modes for the Brink model, using the real topography in Fig. 7a and the measured stratification during a cruise to the region in 2010 (Ha et al, 2014); together with the analytical solution (2) using boundary conditions (4).

The eigenfunction over the real topography (solid lines, Fig. 7a and 7b) has the surface signature of the wave concentrated to the steeper parts of the slope, while the simplified solution (dashed lines, Fig. 7a and 7b) has the wave spread evenly (sinusoidal) over the slope. Apart from this the surface signature is qualitatively similar for the two solutions. The introduction of stratification does not change the solution in any significant way and the surface signature for the solution with stratification and without are indistinguishable. This is expected since the Burger number, i.e. $Bu = \frac{N^2\alpha^2}{f^2}$ (where N is the buoyancy frequency, α is the bottom slope and f is the Coriolis frequency), is less than 0.1. It was shown in Brink (2006) that for $Bu < 1$ the relative importance of stratification is small compared to the shelf geometry and the solutions are similar to the barotropic solutions.

Expression (3) gives the dispersion relation for a free Rossby wave on a constant bottom slope. The corresponding relation can also be calculated numerically from the Brink (2006) model, using the boundary condition (4). Figure 8 shows the numerical solution together with expression (3) for the first two modes.

From the dispersion relation, the group velocity in the x-direction, C_X, is given by

$$c_X = \frac{d\omega}{dk},$$

or (using (3))

$$c_X = \frac{\beta(k^2 - l^2 - \frac{f^2}{gH})}{(k^2 + l^2 + \frac{f^2}{gH})^2}. \qquad (6)$$

Since the topographic variations in the study region are of order 100 km or smaller, we have that $k^2 \gg \frac{f^2}{gH}$ and $l^2 \gg \frac{f^2}{gH}$ (using $k, l \geq \frac{1}{10^5}$, $f \sim 1.4 \cdot 10^{-4}$ s^{-1}, $H \sim 500$ m). Equations (3) and (6) can then be approximated by

$$\omega \simeq -\frac{\beta k}{k^2 + l^2} \tag{7}$$

$$c_X \simeq \frac{\beta (k^2 - l^2)}{(k^2 + l^2)^2}. \tag{8}$$

Expression (8) tells us that for short waves, energy propagates with the coast on the right-hand side, i.e. south-eastward in the present topography (Fig. 1). The energy in long waves (i.e., small *k*) propagates with shallow water on the left. When the wavelength in the x-direction is approximately equal to the wavelength in the y-direction we have that $k \approx l$ and $c_X \simeq 0$. Then the energy does not move away and there will be resonance if waves are formed in, or transmitted into, the area. The approximate frequency ω_R of the resonant oscillations is given by (using (8) and (5))

$$\omega_R \approx \frac{\beta}{2l_n}, \text{ or } \omega_R \approx \frac{\beta L}{\pi(2n+1)}, \tag{9}$$

where n = 0 for the first mode and n = 1 for the second. Using $\beta = \frac{f\alpha}{H}$ the resonant frequency can hence be written

$$\omega_R \approx \frac{f\alpha}{\pi} \frac{L}{H} \tag{10}$$

for the first mode, where *f* is the Coriolis parameter, α the bottom slope, *L* the length of the slope stretch and *H* the average depth (Fig. 7c shows a sketch of the topographic parameters. Note that *H/L* is in general not equal to α).

The observed spectrum peak for the S2 mooring (Fig. 3) lies close to the frequency where topographic Rossby waves have zero group velocity (Fig. 8) suggesting that the observed oscillations might be resonant Rossby waves. These oscillations appear not to affect the average North-Westward flow of water: the wavelet analysis (Fig. 4) shows that oscillations of period around 64 hours or shorter have strong variability but that peaks of energy around this frequency are not coinciding with peaks of energy in lower frequency.

Using the simplified expression (9) and topographic parameters (Fig. 7c) relevant for the three moorings (Table 2), it is seen that the fastest resonant oscillations are occurring at S2 and slower ones (period 83 hours) are expected at S3. The observations show broad sub-inertial peaks centered on somewhat lower frequencies at S3 than S2, in qualitative agreement with the analytical expression (Fig. 3). For S1 the first-mode resonant period is 157 h (6.5 days), likely too slow to permit free waves to form. The wind forcing often changes sign during 157 hours, and in addition the oscillations are slow enough for frictional damping to be effective (Brink, 2006). Nonetheless, on occasion a slow oscillation resembling the persistent ones at S2 and S3 can be seen also in S1.

4. Discussion

The high coherence (0.69) between wind and cross-shelf velocity for a 67 hour period suggests that the observed oscillations are resonant topographic Rossby waves triggered by the wind. A similar resonant interaction has e.g. been observed on the Scottish continental shelf when storms created topographic Rossby waves along the slope (Gordon and Huthnance, 1987) and on the southern slope of the Iceland-Faroe ridge (Miller, Lermusiaux, & Poulain, 1996). The fact that they are so clearly observed in the present study is somewhat surprising, given that no previous reports of resonant topographic Rossby waves have been made from the Antarctic continental shelf. An explanation can be that the topography in this area is steep and shallow such that the first mode Rossby wave has a comparatively high resonant frequency. Semi-regular oscillations with distinct sub-inertial periods have however been found e.g. in the Weddell Sea (Darelius et al, 2008; Jensen et al, 2013) and are not inconsistent with the theory of resonant topographic Rossby waves. The measurements at S2 shows (Fig. 2; see also Ha et al, 2014) that in addition to the resonant waves there is a more slowly varying current out from the shelf, transporting water and heat away from the continent (Ha et al, 2014). However, at any one time the velocity and temperature field is completely dominated by the Rossby waves oscillating on a 60-80 hour time scale. The oscillations are comparable, or even larger, in magnitude to tides (Fig. 3). Single CTD and LADCP measurements are hence of limited value in this region. In order to get an estimate of quantities important for oceanic heat flux to glaciers, such as warm layer thickness, heat transport or bottom temperature it is imperative to measure during at least one Rossby cycle (i.e. about 80 hours). This is particularly important when drawing conclusions of long-term trends based on sparse CTD measurements.

It is also important to distinguish these resonant Rossby waves from eddies. Both waves and eddies have oscillations in velocity and temperature/salinity, although eddies are less regular. However, eddies arise from an instability in the main flow and act to transport fluid parcels across gradients in depth, density or velocity to ultimately stabilize the flow. For example eddy-induced transport is a primary contributor to mass and property fluxes across the slope in the West Antarctic Peninsula (see e.g. Thompson et al, 2014; Moffat et al, 2009; Martinson and McKee, 2012). Single linear Rossby waves on the other hand are triggered by external events, e.g. wind bursts, and have no impact on the mean flow. Hence, although there is a clear correlation between velocity and temperature, the waves found in the present study does not induce any net oceanic heat flux towards or away from the coast. This is expected since waves per definition does not move any fluid and have closed streamlines. If the waves break, e.g. when they encounter small-scale topography, or if multiple waves occur at the same time, a net transport in the cross-shelf direction (e.g. StLaurent et al, 2013). Such effects are however second order compared to the pronounced lifting/dropping of the thermocline that the oscillations themselves induce.

References

Arndt, J.E., H. W. Schenke, M. Jakobsson, F. Nitsche, G. Buys, B. Goleby, M. Rebesco, F. Bohoyo, J.K. Hong, J. Black, R. Greku, G. Udintsev, F. Barrios, W. Reynoso-Peralta, T. Morishita, R. Wigley, 2013. The International Bathymetric Chart of the Southern Ocean (IBCSO) Version 1.0 - A new bathymetric compilation covering circum-Antarctic waters, Geophysical Research Letters, doi: 10.1002/grl.50413

Arneborg, L., Wåhlin, A. K., Björk, G., Liljebladh, B., & Orsi, A. H. (2012). Persistent inflow of warm water onto the central Amundsen shelf. *Nature Geoscience*, *5*(12), 876–880. doi:10.1038/ngeo1644

Cartwright, D. E., J. M. Huthnance, R. Spencer, and J. M. Vasse, 1980. On the St Kilda Shelf Tidal Regime. Deep Sea Research, 27, 61 - 70.

Gill, A., 1986: Atmosphere–Ocean Dynamics. Academic Press, 662 pp.

Gordon, R. L., & Huthnance, J. M. (1987). Storm-driven continental shelf waves over the Scottish continental shelf. *Continental Shelf Research*, *7*(9), 1015–1048.

Ha, H. K., Wåhlin, A., T. W. Kim, S. H. Lee, J. H. Lee, H. J. Lee, C. S. Hong, L. Arneborg, G. Björk & O. Kalén, 2014. Circulation and Modification of Warm Deep Water on the Central Amundsen Shelf. Journal of Physical Oceanography, 44, 1493 - 1501. DOI: 10.1175/JPO-D-13-0240.1

Jacobs, S., A. Jenkins, C. Giulivi and P. Dutrieux, 2011. Stronger ocean circulation and increased melting under Pine Island Glacier ice shelf. Nature Geoscience, 4, 519 - 523.

Jenkins, A., P. Dutrieux, S. Jacobs, S. McPhail, J. Perrett, A. Webb and D. White, 2010. Observations beneath Pine Island Glacier in West Antarctica and implications for its retreat. Nature Geoscience, 3, 468 - 472.

Jensen, M. F., Fer, I., & Darelius, E. (2013). Low frequency variability on the continental slope of the southern Weddell Sea. *Journal of Geophysical Research: Oceans*, *118*. doi:10.1002/jgrc.20309

Marques, G. M., Padman, L., Springer, S. R., Howard, S. L., & Özgökmen, T. M. (2014). Topographic vorticity waves forced by Antarctic dense shelf water outflows. *Geophysical Research Letters*, *41*(4), 1247–1254. doi:10.1002/2013GL059153

Martinson, D. G., and D. C. McKee, 2012: Transport of warm Upper Circumpolar Deep Water onto the western Antarctic Peninsula continental shelf. Ocean Sci., 8, 433–442, doi:10.5194/os-8-433-2012.

Miller, Lermusiaux, and Poulain, 1996. A topographic Rossby-mode resonance over the Iceland-Faroe ridge. Journal of Physical Oceanography, 26, 2735 - 2747.

Moffat, C., B. Owens, and R. C. Beardsley, 2009: On the characteristics of Circumpolar Deep Water intrusions on the west Antarctic Peninsula continental shelf. J. Geophys. Res., 114, C05017, doi:10.1029/2008JC004955.

Padman, L., Plueddemann, A. J., Muench, R. D., & Pinkel, R. (1992). Diurnal tides near the Yermak Plateau. *Journal of Geophysical Research*, *97*(92), 639–652. doi:doi:10.1029/92JC01097

Pawlowicz, R., B. Beardsley, and S. Lentz, 2002: Classical tidal harmonic analysis including error estimates in MATLAB using T_TIDE. Comput. Geosci., 28, 929–937.

Pritchard, H. D. *et al.* Antarctic ice-sheet loss driven by basal melting of ice shelves. *Nature* **484**, 502–505 (2012).

StLaurent, P., Klinck, J. and M. Dinniman, 2013. On the Role of Coastal Troughs in the Circulation of Warm Circumpolar Deep Water on Antarctic Shelves. Journal of Physical Oceanography, 43, 51 - 64. DOI: 10.1175/JPO-D-11-0237.1

Thompson, A., Heywood, K., Schmidtko, S. and Stewart, a., 2014. Eddy transport as a key component of the Antarctic overturning circulation. Nature Geoscience, DOI: 10.1038/NGEO2289

Thompson, A. 2008. The atmospheric ocean: Eddies and jets in the Antarcitc Circumpolar Current. Phil. Trans. R. Soc. A, 366, 4529-4541

Torrence, C. and Compo, G. 1997. A practical guide to wavelet analysis. *Bull. Am. Meteorol. Soc.* **79**, 61–78.

Uppala et al., 2005: The ERA-40 re-analysis. *Q. J. R. Meteorol. Soc.*, 131, 2961-3012.

Vangriesheim, A., Marie Treguier, A., & Andre, G. (2005). Biweekly current oscillations on the continental slope of the Gulf of Guinea. *Deep Sea Research Part I: Oceanographic Research Papers*, *52*(11), 2168–2183. doi:10.1016/j.dsr.2005.05.010

Wåhlin, A. K., Yuan, X., Björk, G., & Nohr, C. (2010). Inflow of Warm Circumpolar Deep Water in the Central Amundsen Shelf*. *Journal of Physical Oceanography*, *40*(6), 1427–1434. doi:10.1175/2010JPO4431.1

Wåhlin, A., O. Kalén, L. Arneborg, G. Björk, G. Carvajal, H. K. Ha, T. W. Kim , S. H. Lee, J. H. Lee, C. Stranne, 2013. Variability of Warm Deep Water Inflow in a Submarine Trough on the Amundsen Sea Shelf. Journal of Physical Oceanography, 43, 2054 - 2010.

Walker, D. P. et al. Oceanic heat transport onto the Amundsen Sea shelf through a submarine glacial trough. Geophys. Res. Lett. 34, L02602 (2007).

Table 1: Mooring: coordinates, depth, deployment periods and instrumentation. The ADCP's were both 150-kHz instruments from RDI deployed upward-looking at the bottom to measure current velocity profiles. The observed velocity data were processed using the WinADCP® software. The MicroCATs on S3 unfortunately stopped recording data in January 2013.

Mooring	Latitude	Longitude	Depth	Depl	Recov	ADCP	MicroCATs
S1	72º 27.279' S	116º 20.92' W	584 m	2010-02-15	2012-03-01	Y	5-7
S2	73º 0.94' S	117º 14.86' W	614 m	2010-12-25	2012-02-11	Y	6
S3	72º 55.60' S	117º 34.75' W	578 m	2012-03-01	2014-01-25	N	3

Table 2: Approximate topographic parameters for the three mooring sites, based on bathymetric data from the IBCSO data base (Arndt et al, 2013). In the table, α denotes bottom slope, L denotes distance between the trough crest and the trough bottom and H_0 is the depth at the trough crest (see sketch in Fig. 7c). Also shown are the calculated frequencies ω_R for the first two modes of resonant topographic Rossby waves (expression (10)) and the corresponding periods T_R .

Mooring	α	L	H_0	H	ω_R^1 (rad/s)	ω_R^2 (rad/s)	T_R^1 (h)	T_R^2 (h)
S1	0.001	100 km	350 m	400 m	$1.1 \cdot 10^{-5}$	$3.7 \cdot 10^{-6}$	157 h	470 h
S2	0.01	45 km	250 m	475 m	$4.2 \cdot 10^{-5}$	$1.4 \cdot 10^{-5}$	41 h	124 h
S3	0.005	45 km	370 m	480 m	$2.1 \cdot 10^{-5}$	$6.7 \cdot 10^{-6}$	83 h	250 h

Figure captions

Figure 1: Map of the region with all moorings, together with mooring setup (right panel) Map of the study region with the moorings S1, S2 and S3. The orange arrows show the rotation of the velocities to fit the orientation of the channel, with U as the along-trough velocity and V the cross-trough velocity. The red and purple lines with arrows depict the general circulation pattern and cooling of the warm deep-water (Ha et al., 2014). Bathymetry is from Arndt et al. (2013).

Figure 2. Velocity, temperature and salinity from mooring S2. The four panels show hourly averaged data according to color bars as a function of time and depth. (a) detided along-channel velocity (positive in the South-Eastward direction, i.e. towards the continent), (b) detided across-channel velocity (positive in the North-Eastward direction, i.e. down the slope), (c) temperature and (d) salinity. Black triangles in (c) and (d) show the approximate positions of the MicroCATs.

Figure 3. Fourier spectra (black lines) and rotary spectra (grey lines) of velocity data from S2, 100 mab. Red lines show the frequency for zero group velocity according to the numerical model in Brink (2006)

Figure 4: Results from wavelet analysis of data from mooring S2 (a) Along-channel velocity, vertical average (b) Across-channel velocity, vertical average (c) Temperature, bottom value. Red color indicates high energy levels and blue low levels. The bold black contours are the 95% confidence levels. Values outside cone of influence (parabolic black contour) are not plotted. The arrow in panel (a) show the time of the oscillations in Fig. 5

Figure 5. Oscillations in velocity and temperature. (a) Detided across-trough velocity component (b) Detided along-trough velocity component (c) Temperature (d) Quiver-plot showing lowpassed velocity anomalies from S2, 100 mab. The velocity scale is given in the lower left corner and the color of the arrow indicates the temperature at 100 mab. The dashed, black line indicates the direction of the trough. Dates are given in the format month/day.

Figure 6. Time series of temperature from the three MicroCATs at mooring S3. For location of the mooring see Figure 1 and Table 1. (a) Complete record (b) Example of oscillations occurring between days 128 - 145 (c) Example of oscillations occurring between days 185 - 202. Color indicate MicroCAT depth according to legend in (a).

Figure 7. (a) Real topography (shaded area) as measured by multibeam on the IB Oden during a cruise to the region in 2010, together with a straight dotted line representing the simplified topography used for analytical solutions. (b) The mode structures obtained from the analytical solution (dotted lines) and the numerical solution obtained using the real bathymetry and stratification (solid lines). The black lines show the first mode, the red lines show the second mode. (c) Sketch showing the topographic parameters in the analytical expressions and for the calculations of the resonant frequencies in Table 2.

Figure 8. Dispersion relation for the analytical solution (dotted lines) and the numerical solution based on real topography and stratification (solid lines). Black lines show first mode, red lines show second mode. The shaded square indicates the frequency boundaries of the observed

spectrum peak (see Fig. 3) and the wavelength boundaries (green lines in Fig. 7). Red circle indicate the zero group velocity frequency-wavelength combination used.

Figures

Figure 1

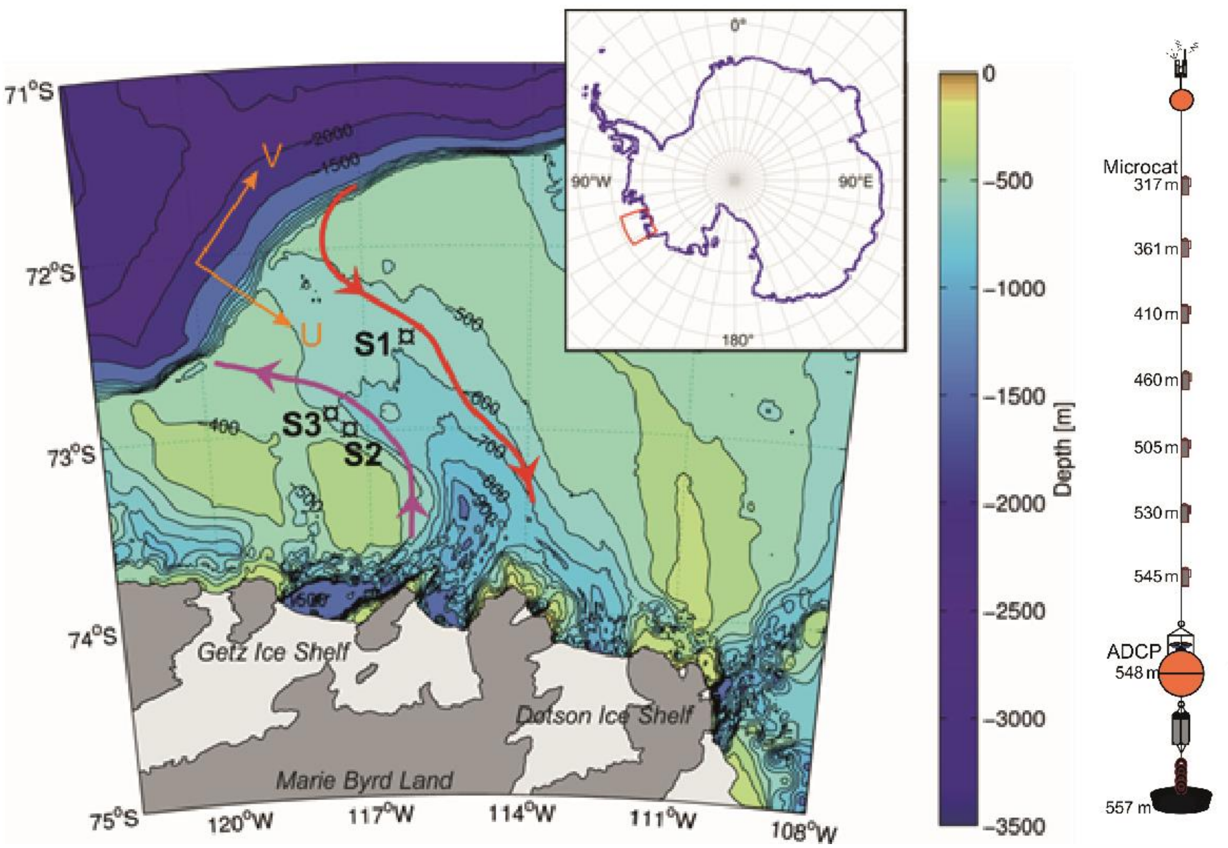

Figure 1: Map of the region with all moorings, together with mooring setup (right panel)

Map of the study region with the moorings S1, S2 and S3. The orange arrows show the rotation of the velocities to fit the orientation of the channel, with U as the along-trough velocity and V the cross-trough velocity. The red and purple lines with arrows depict the general circulation pattern and cooling of the warm deep-water (Ha et al., 2014). Bathymetry is from Arndt et al. (2013).

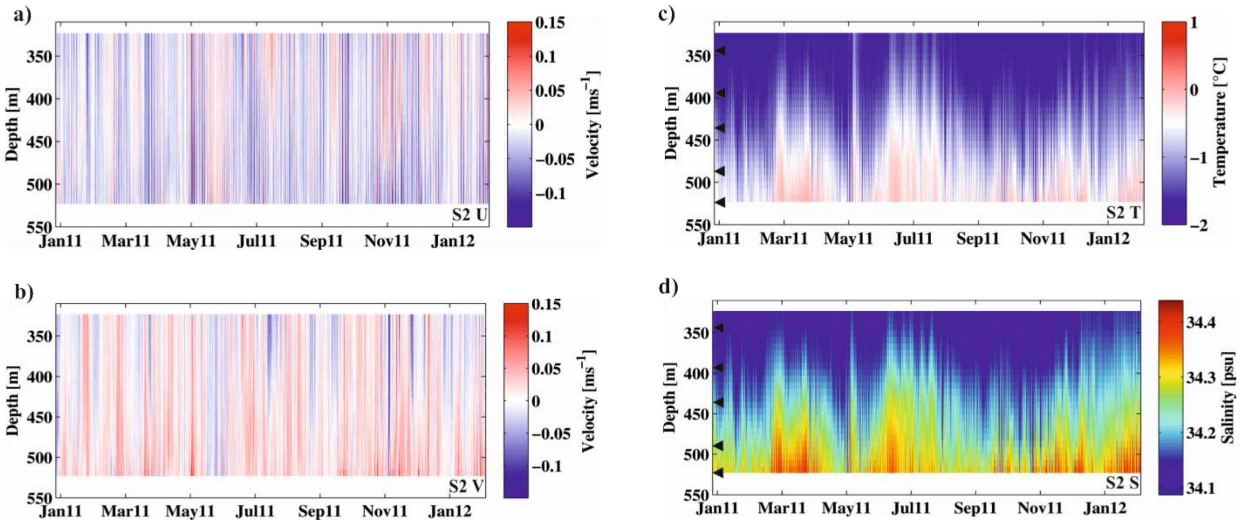

Figure 2. Velocity, temperature and salinity from mooring S2. The four panels show hourly averaged data according to color bars as a function of time and depth. (a) detided along-channel velocity (positive in the South-Eastward direction, i.e. towards the continent), (b) detided across-channel velocity (positive in the North-Eastward direction, i.e. down the slope), (c) temperature and (d) salinity. Black triangles in (c) and (d) show the approximate positions of the MicroCATs.

Figure 3

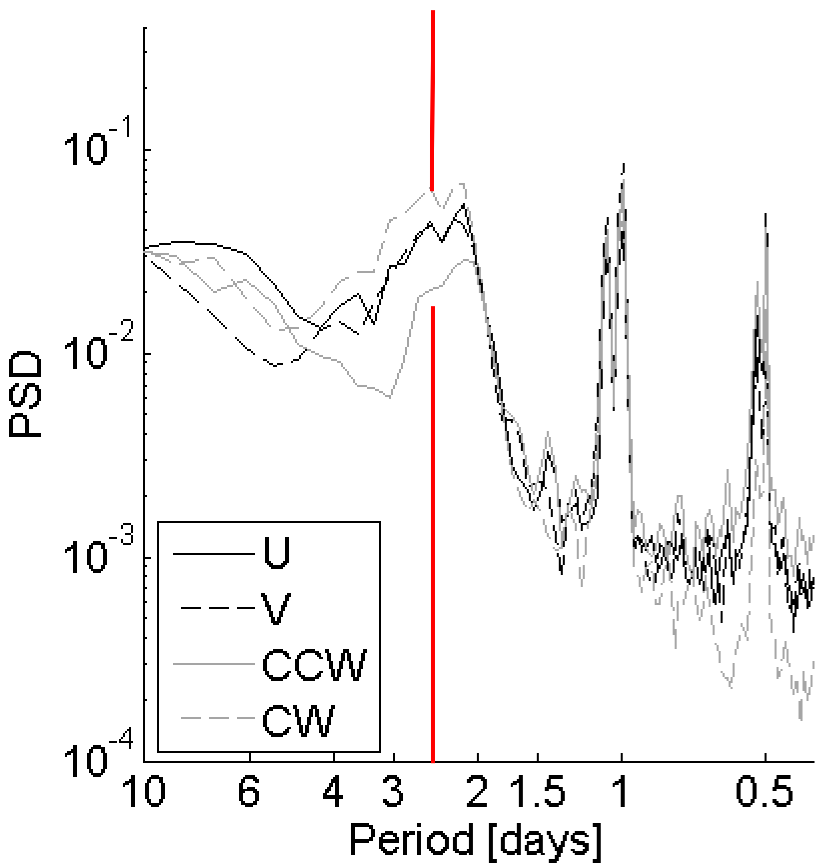

Figure 3. Fourier spectra (black lines) and rotary spectra (grey lines) of velocity data from S2, 100 mab. Red lines show the frequency for zero group velocity according to the numerical model in Brink (2006)

Figure 4

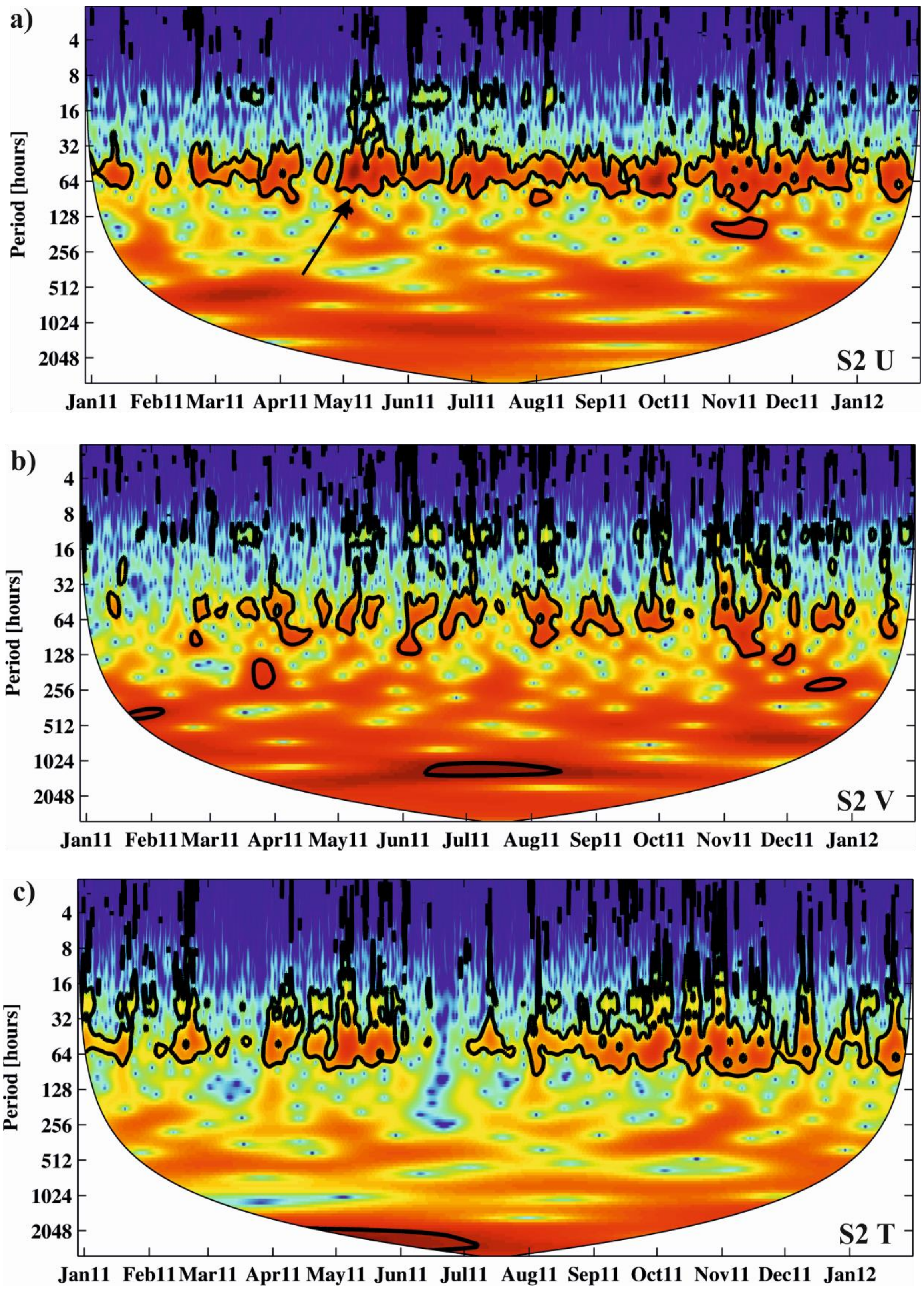
a)
Period [hours]
4
8
16
32
64
128
256
512
1024
2048
S2 U
Jan11 Feb11 Mar11 Apr11 May11 Jun11 Jul11 Aug11 Sep11 Oct11 Nov11 Dec11 Jan12
b)
Period [hours]
4
8
16
32
64
128
256
512
1024
2048
S2 V
Jan11 Feb11 Mar11 Apr11 May11 Jun11 Jul11 Aug11 Sep11 Oct11 Nov11 Dec11 Jan12
c)
Period [hours]
4
8
16
32
64
128
256
512
1024
2048
S2 T
Jan11 Feb11 Mar11 Apr11 May11 Jun11 Jul11 Aug11 Sep11 Oct11 Nov11 Dec11 Jan12

Figure 4: Results from wavelet analysis of data from mooring S2 (a) Along-channel velocity, vertical average (b) Across-channel velocity, vertical average (c) Temperature, bottom value. Red color indicates high energy levels and blue low levels. The bold black contours are the 95% confidence levels. Values outside cone of influence (parabolic black contour) are not plotted. The arrow in panel (a) show the time of the oscillations in Fig. 5

Figure 5

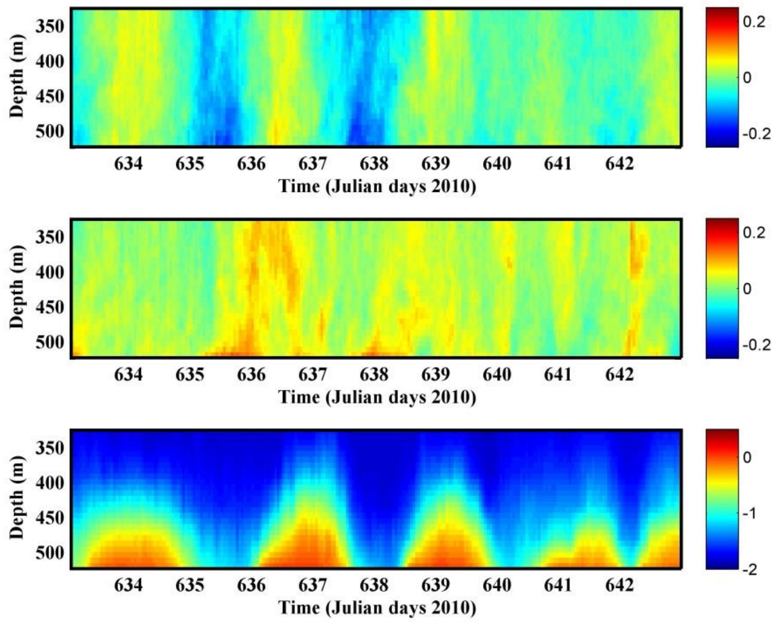

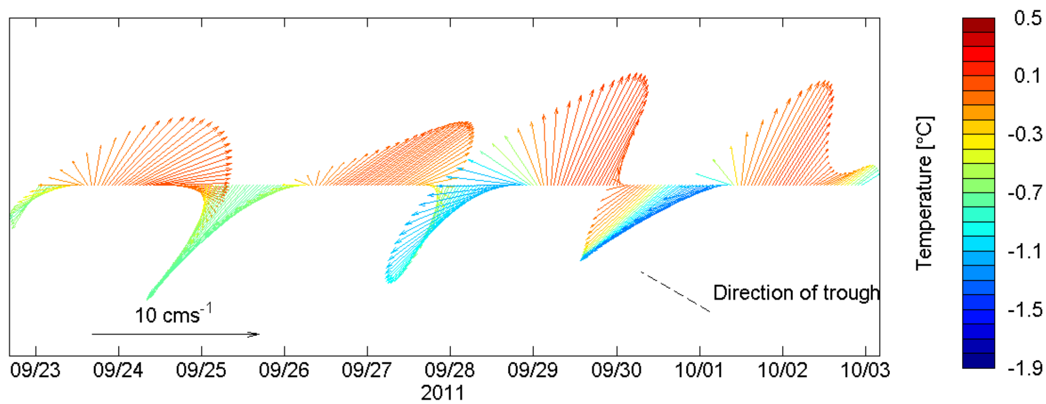

Figure 5. Oscillations in velocity and temperature. (a) Detided across-trough velocity component (b) Detided along-trough velocity component (c) Temperature (d) Quiver-plot showing lowpassed velocity anomalies from S2, 100 mab. The velocity scale is given in the lower left corner and the color of the arrow indicates the temperature at 100 mab. The dashed, black line indicates the direction of the trough. Dates are given in the format month/day.

Figure 6

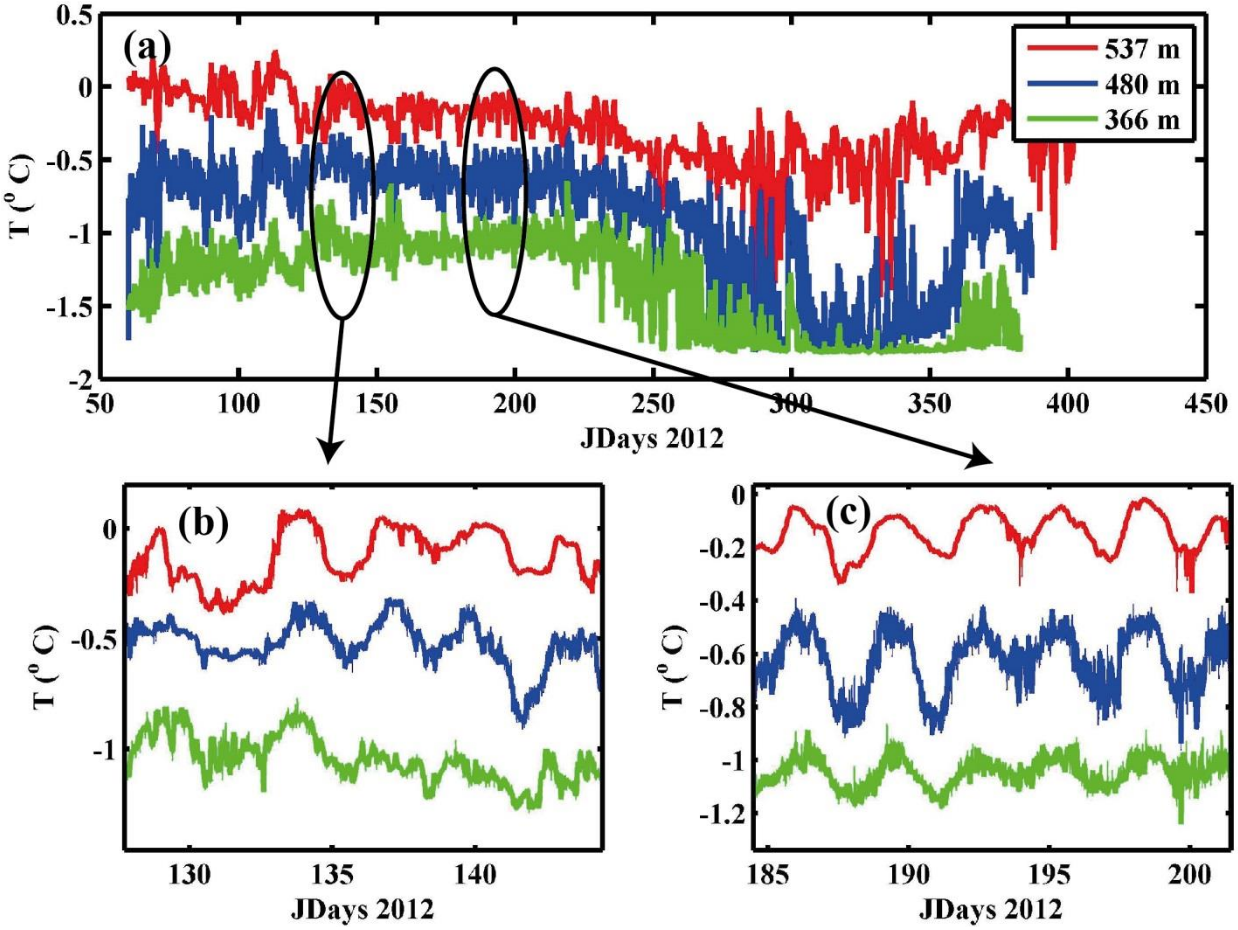

Figure 6. Time series of temperature from the three MicroCATs at mooring S3. For location of the mooring see Figure 1 and Table 1. (a) Complete record (b) Example of oscillations occurring between days 128 - 145 (c) Example of oscillations occurring between days 185 - 202. Color indicate MicroCAT depth according to legend in (a).

Figure 7

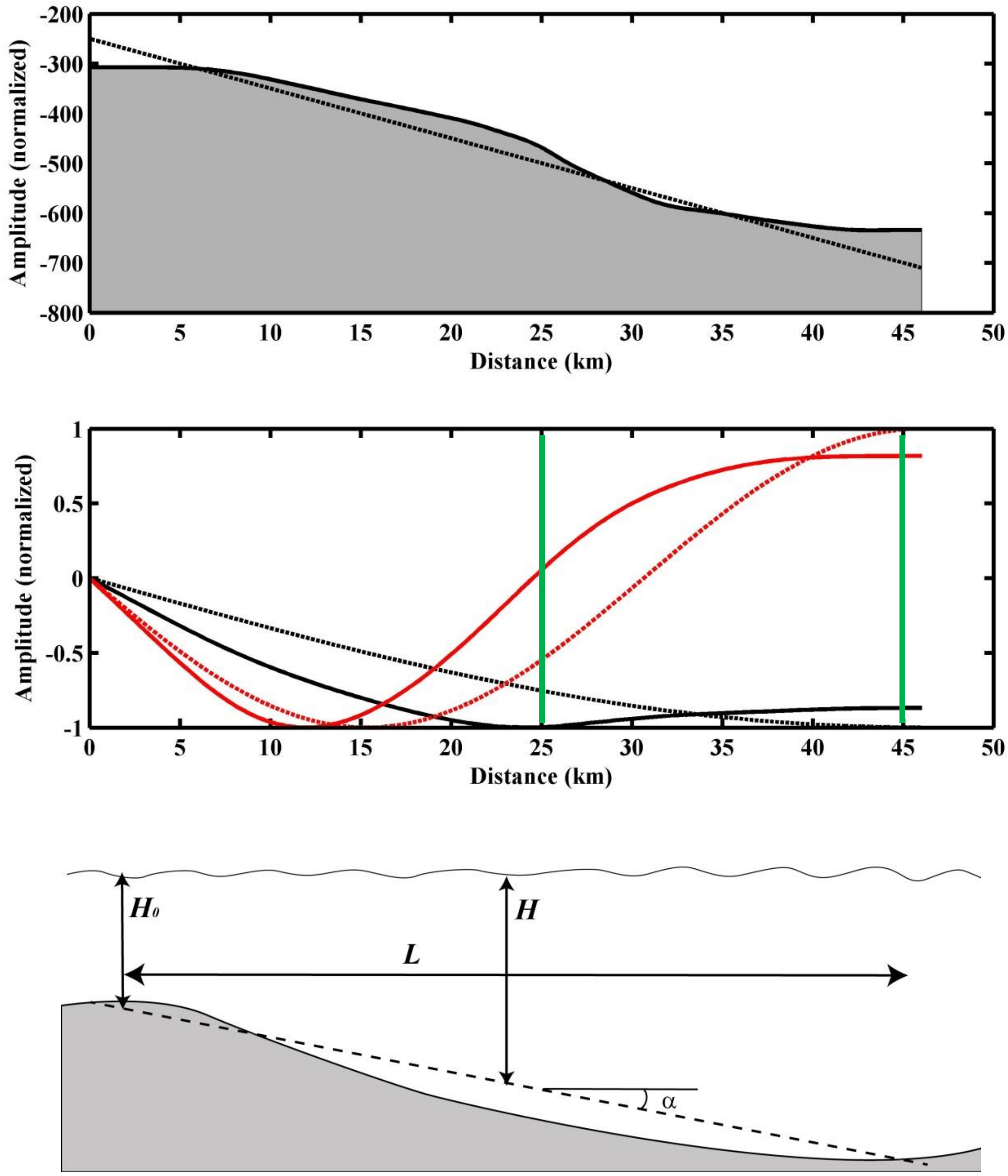

Figure 7. (a) Real topography (shaded area) as measured by multibeam on the IB Oden during a cruise to the region in 2010, together with a straight dotted line representing the simplified topography used for analytical solutions. (b) The mode structures obtained from the analytical solution (dotted lines) and the numerical solution obtained using the real bathymetry and

stratification (solid lines). The black lines show the first mode, the red lines show the second mode. (c) Sketch showing the topographic parameters in the analytical expressions and for the calculations of the resonant frequencies in Table 2.

Figure 8

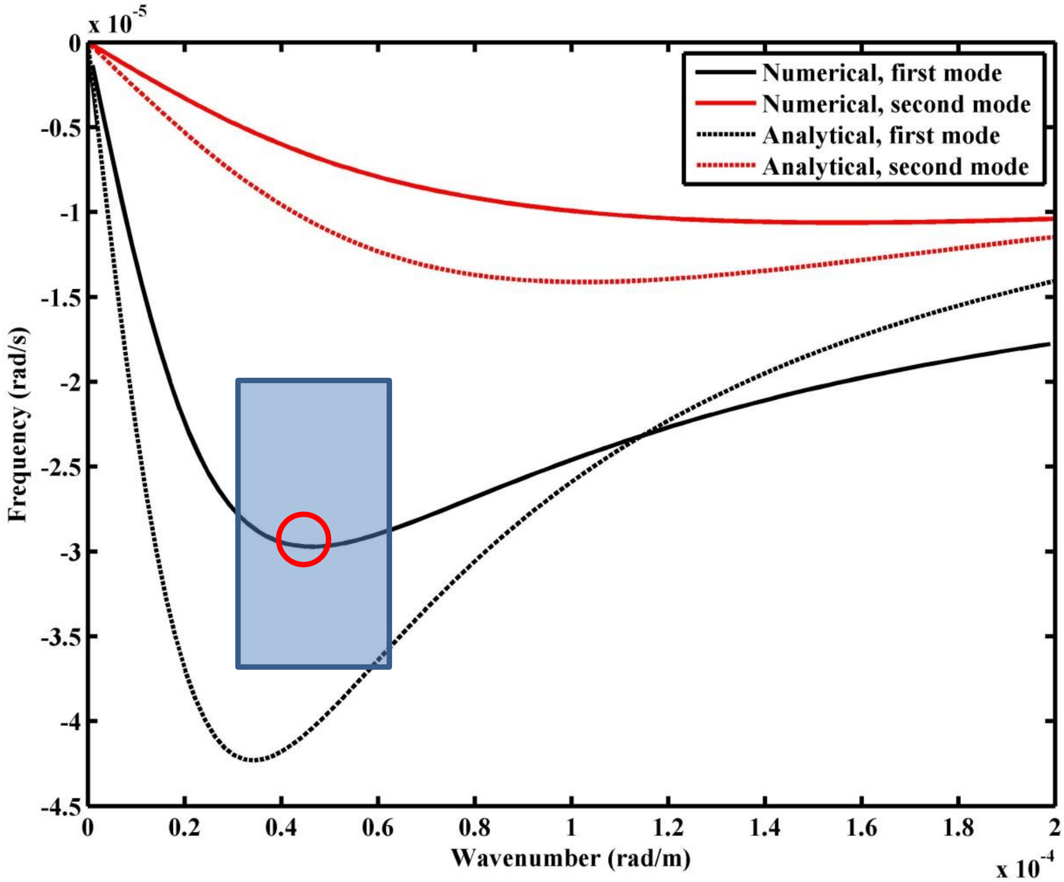

Figure 8. Dispersion relation for the analytical solution (dotted lines) and the numerical solution based on real topography and stratification (solid lines). Black lines show first mode, red lines show second mode. The shaded square indicates the frequency boundaries of the observed spectrum peak (see Fig. 3) and the wavelength boundaries (green lines in Fig. 7). Red circle indicate the zero group velocity frequency-wavelength combination used.